THE ASTROPHYSICAL JOURNAL, 308:357–369, 1986 September 1

THE SIZE SPECTRUM OF MOLECULAR CLOUDS IN THE OUTER GALAXY

SUSAN TEREBEY
High Altitude Observatory and Advanced Study Program, National Center for Atmospheric Research
MICHEL FICH
University of Washington
LEO BLITZ
University of Maryland
AND
CHRISTIAN HENKEL
Max-Planck-Institut für Radioastronomie and AT & T Bell Laboratories
Received 1985 October 14; accepted 1986 February 13

ABSTRACT

We present a technique for determining the molecular cloud size spectrum that corrects for incompleteness in the observational data. We apply the method to a survey of molecular clouds in the Outer Galaxy that used the $J = 1$–0 spectral line of ^{12}CO. The fields observed were near the Galactic positions $l = 125°$, $b = 2°$ and $l = 220°$, $b = -2°$. A total of 16 molecular clouds ranging from 2 to 45 pc in size were detected.

Models that correct for the incompleteness of the survey are compared with the molecular cloud data. The best-fitting size spectrum is determined by using the maximum likelihood method, while the reliability of the fit is estimated by using the Kolmogorov-Smirnov small-number statistic. Two different rotation curves are used, in order to indicate the level of sensitivity of the fit to the choice of rotation curve.

When kinematic distances are assigned using the Blitz, Fich, and Stark (1980) rotation curve, or a flat rotation curve, the best-fitting cloud size spectrum has a power-law exponent of $-2.6(+1.9\ -0.7)$ or $-2.8(+1.3\ -1.0)$, respectively, where the 90% confidence limits are as indicated.

The measurements of the molecular cloud size spectrum fall within the range of values reported in the inner Galaxy and are close to measurements of the local H I cloud size spectrum. The simplest interpretation is that one physical mechanism is responsible for cloud formation. Given this interpretation, then, the decline in the ratio of H_2 to H I surface densities by roughly an order of magnitude between the peak of the molecular ring and the outer Galaxy suggests that (1) the cloud formation process is substantially independent of whether the interstellar gas is in atomic or molecular form and (2) most of the interstellar mass is contained in the largest clouds. Near the peak of the molecular ring, much of the gas is found in giant molecular clouds; in the outer Galaxy we would expect giant H I complexes to contain most of the mass.

Subject headings: galaxies: internal motions — galaxies: Milky Way — galaxies: structure — interstellar: molecules

I. INTRODUCTION

Observations of the outer Galaxy have the potential to tell us a great deal about the physical processes that are important in star formation and the formation of molecular clouds. Over the range from the well-studied inner portions of the Galaxy using ^{12}CO, H I, and H II regions (Burton 1976; Burton and Gordon 1978; Lockman 1979; Robinson *et al.* 1984; Sanders, Solomon, and Scoville 1984) to the outer Galaxy (Henderson, Jackson, and Kerr 1982; Kulkarni, Blitz, and Heiles 1982; Fich and Blitz 1984; Sanders, Solomon, and Scoville 1984), there is a significant global variation in important physical parameters such as the molecular gas surface density and gas scale heights. In brief, the azimuthally averaged surface density of molecular gas has a peak near 6 kpc in the "molecular ring" and decreases sharply and monotonically outward. In contrast, the H I gas surface density is nearly constant from about 4 kpc to 18–20 kpc with the surface densities of the molecular and atomic gas crossing somewhere inside the solar circle. The scale height of the gas is fairly constant from 4 to 10 kpc in both ^{12}CO and H I, but increases outside the solar circle in H I by a factor of about 3 out to 18–20 kpc. Clemens (1985) finds no evidence for variations in the cloud-cloud random velocities throughout the inner Galaxy.

The apparent low density of molecular clouds measured in the outer Galaxy implies that it is a harsh environment for the formation of molecular gas. In trying to understand the cause of the variation in the global molecular gas distribution, it becomes important to determine how other cloud properties such as the cloud size spectrum and cloud mass may vary throughout the Galaxy. Comparison of this information with theory will lead to better understanding and development of global models of star formation (e.g., Guibert, Lequeux, and Viallefond 1978).

A number of workers have measured the molecular cloud size or mass spectrum in the inner Galaxy (Solomon, Sanders, and Scoville 1979; Liszt, Xiang, and Burton 1981; Sanders, Scoville, and Solomon 1985) and in the Perseus arm near the solar circle (Casoli, Combes, and Gerin 1984). The derived or inferred mass spectra imply that in terms of logarithmic mass size intervals, the mass in molecular clouds is a slowly increasing function of cloud mass. Although the results of various groups tend to agree reasonably well, there are a number of selection effects that may introduce biases into the results: the near-far ambiguity of kinematically assigned distances interior to the solar circle, the line blending of spatially unrelated cloud emission especially near the tangent point in the inner Galaxy, and incompleteness in the surveys.

We have developed a technique to derive the cloud size spectrum that corrects for the incompleteness of molecular cloud surveys. We have mapped two regions in the outer Galaxy in order to test the method and also to investigate how molecular clouds in the outer Galaxy differ from their inner Galaxy counterparts. By working in the outer Galaxy we avoid the near-far distance ambiguity that has plagued other surveys. In addition, the low density of molecular clouds ensures that accidental line blending is not a problem. Our analysis pays careful attention to the biases in our survey as well as to the statistical significance of our results. In order to examine systematic effects on the results we have assigned kinematic distances using two different rotation curves, that of Blitz, Fich, and Stark (1980, hereafter BFS) and a flat rotation curve outside the solar circle with velocity parameters $R_{\odot} = 10$ kpc and $\theta_{\odot} = 250$ km s^{-1}. Some recent work (Fich and Blitz 1986) derives an outer Galaxy rotation curve that has properties intermediate between the two.

In § II we discuss the design of the survey and the molecular clouds that were detected. The large-scale structure found is discussed in § III, using at most an assumed rotation curve to interpret the data. We derive the cloud size spectrum from a comparison of our cloud sample with a calculated model. The technique is presented in § IV, where the incompleteness correction and the assumed model for the outer Galaxy are described, while the results for the cloud size spectrum can be found in § V. Readers who are mainly interested in the results are directed to §§ II and V and the discussion in § VI.

II. OBSERVATIONS

a) Instrument and Calibration

Most of the data were taken with the NRAO[1] 36 foot (11 m) telescope on Kitt Peak during the periods 1982 January 4–10 and May 22–27. The telescope was operated in double-sideband spectral line mode at the frequencies of the $J = 1$–0 ^{12}CO transition at 115.3 GHz and the $J = 1$–0 ^{13}CO transition at 110.2 GHz.

The two receivers were operated in parallel to increase the sensitivity. The filter-bank configuration provided 128 channels at 250 kHz resolution and 128 channels at 500 kHz resolution, giving a velocity coverage of 83 and 166 km s^{-1} and a velocity resolution of 0.65 and 1.3 km s^{-1}, respectively.

The data were taken by position switching with respect to a small number of fixed reference positions. Typical integration times varied from 1 to 4 minutes.

Calibration was done using the chopper-wheel method. Antenna temperatures are expressed in terms of $T_R{}^*$, as defined by Kutner and Ulich (1981). A discussion of the telescope parameters and calibration during the period when the observations were made can be found in Kutner, Mundy, and Howard (1984).

The measured antenna temperatures were multiplied by a correction factor to compensate for the attenuation of the sunscreen and the double-sideband instead of single-sideband mode of observation. The correction factors used (Howard 1982) are 0.93 for the quasi-optics box without single-sideband rejection filter, 1.11 for the sunscreen, 1.05 for the vane heated above ambient temperature (varies with ambient temperature), and 1.07 for the gain of the image to signal sideband for the two receivers, leading to a net correction of 1.16.

To check the calibration we observed the standard sources Orion A (60 K), S146 (13.2 K),W51 (28.4 K), and W3OH (16.0 K) (Ulich and Haas 1976). We also monitored two H II regions that were near our fields, S187 and S287, every few hours, to check for consistency. The average measured intensity of the standard sources was 0.93 times the quoted values, with an rms variation of 12%; the internal rms variations of S187 and S287 were similar. It should be kept in mind that many of the detected lines have antenna temperatures that are only 3 or 4 times the rms noise level in a single channel and therefore have a large noise contribution.

At the frequency of ^{12}CO the telescope beam is 1'.1 FWHM. Use of the sunscreen led to small differences in the pointing. From monitoring of pointing calibration sources we estimate the pointing to be accurate to 0'.2–0'.3 rms.

In addition to the NRAO millimeter-wave telescope data, some ^{12}CO data of higher sensitivity were obtained with the 7 m offset Cassegrain antenna (FWHM 1'.7) at AT & T Bell Laboratories on 1983 April 13 and 30. The single-sideband data were collected in position switching mode with a spectrometer consisting of 256 1 MHz and 256 250 kHz channels operated in parallel. The beam efficiency was 90%. Calibration and pointing accuracies were $\pm 10\%$ and $\pm 25''$, respectively.

b) Fields Observed

The design of the experiment was to observe two fields, one near Galactic coordinates $l = 125°$, $b = 2°$ and one near $l = 220°$, $b = -2°$. No attempt was made to pick directions that contained peaks in the H I gas or previously observed CO, and in that sense the fields are unbiased. The latitudes were chosen to give a long path length under the assumption that the CO would follow the H I mean midplane. Two different grid spacings were used with the 1'.1 telescope beam, a coarse 4' and a fine 1' spacing in the two different fields. The sensitivity level was increased partway through the survey in order to detect more of the weak lines characteristic of the region. The average rms noise levels of the high and low-sensitivity portions of the survey were 0.45 and 0.82 K, respectively.

A total of 621 grid points at 4' spacing and 486 grid points at 1' spacing were observed in the second quadrant. A total of 150 grid points at 4' spacing and 391 grid points at 1' spacing were observed in the third quadrant. A diagram of the positions observed and typical rms noise levels is shown in Figure 1. In addition, latitude strips were observed at $l = 216°$, 218°, 220°, 236° and with the Bell Laboratories telescope at $l = 124°.2$ and $l = 125°$.

c) Detection Rate

For our survey we find that the observed detection rate for ^{12}CO lines increases with increasing sensitivity, as is shown in Figure 2, where the ratio of number of line detections to observations is plotted against rms noise level. In order to use as spatially uniform a sample as possible, only second-quadrant observations are included. Some of the variation in the figure may be due to actual differences in the number of clouds at the different positions observed. However, this possible bias is likely to be small, since the longitude range is less than 2° and

[1] The National Radio Astronomy Observatory is operated by Associated Universities, Inc., under contract to the National Science Foundation.

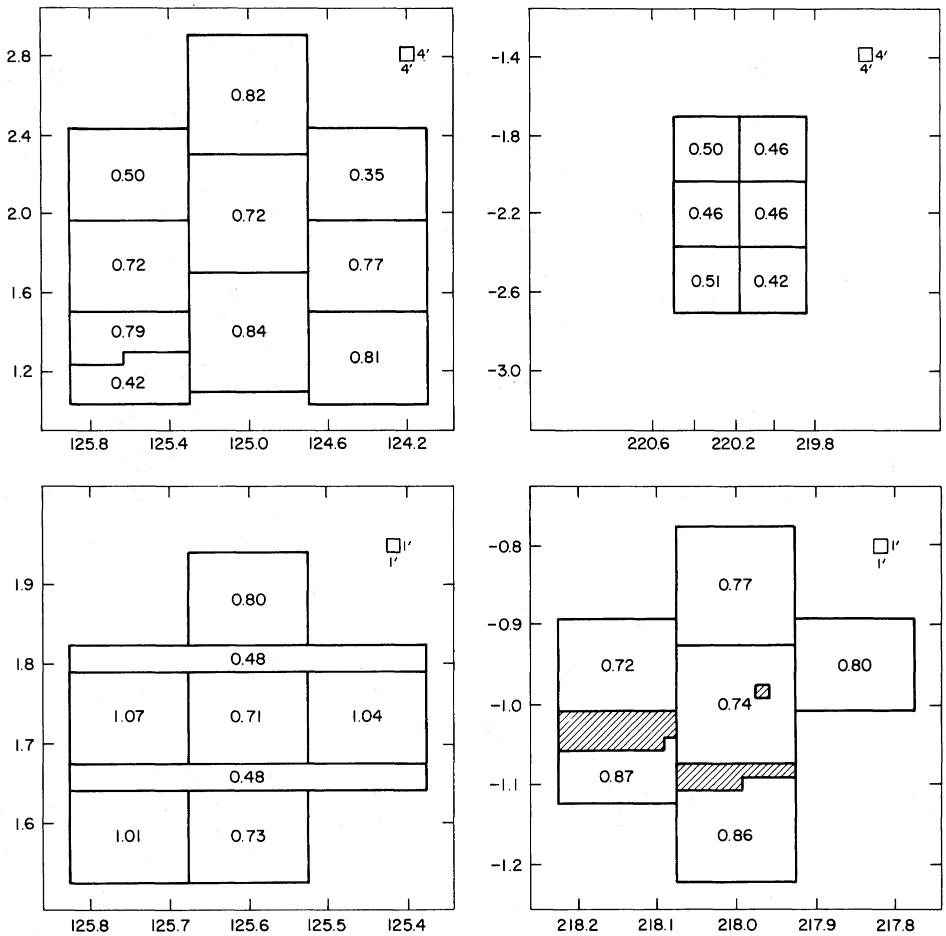

FIG. 1.—Coverage of the survey is shown in Galactic coordinates. Areas near $l = 125°$ and $l = 220°$ were mapped with 4′ or 1′ spacings. The average rms noise level is displayed for each outlined region.

the latitude coverage is similar for the different noise levels. Because of the size of the error bars, it is unclear whether the detection rate has begun to level off or will continue to rise for noise levels below 0.12 K.

d) *Molecular Clouds*

A total of 16 clouds were found that are more than 1 kpc distant. Our detection criterion for a candidate cloud required that the observed intensity be greater than 3 times the rms noise level in at least two adjacent frequency channels. A cloud was considered confirmed if either (1) there was a detection at a nearby position or (2) reobservation of the position showed a positive detection. Some small clouds found in the 4′ survey were mapped with a finer spacing. Local clouds (with distances less than 1 kpc) are not included in the analysis, both because of their large angular size compared with the survey area and because of the large uncertainties in their kinematic distances.

The cloud data are tabulated in Table 1. Some parameters, such as $\langle T_R{}^* \rangle$ and $\langle T_R{}^* \Delta V \rangle$, are defined as averages over the cloud emission and so depend on the rms noise level. Despite the dependence on noise level, these averages can be useful in making comparisons of $T_R{}^*$ and ΔV between clouds and within each cloud.

Table 2 lists the derived properties of cloud diameter $\mathfrak{d}$, line-of-sight distance r, and galactocentric radius R for both the BFS and flat rotation curves. Lower limits on the diameter are given for clouds on the survey boundaries whose extents were

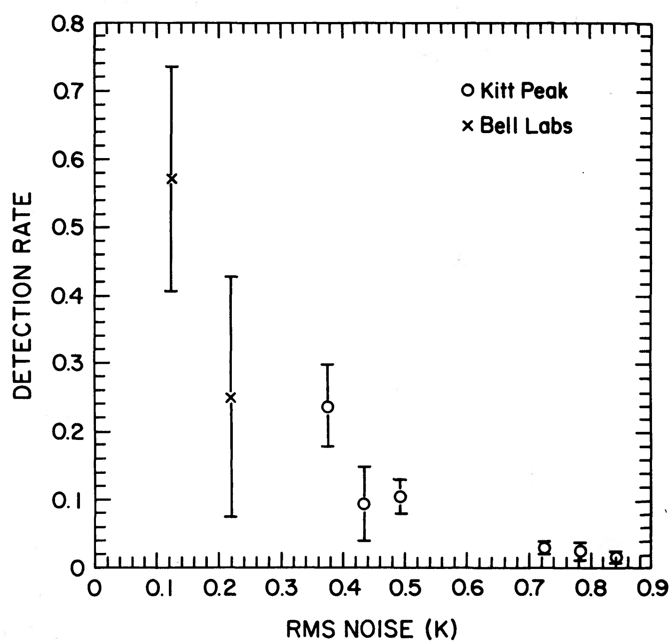

FIG. 2.—Fractional detection rate of spectral lines plotted against the rms noise level; $\sqrt{N}$ error bars are shown, where N is the number of lines detected. Kitt Peak and Bell Laboratories data near $l = 125°$, $b = 2°$ are included in the figure. Local emission lines ($|V_r| < 15$ km s^{-1}) are excluded. Very weak lines are characteristic in the outer Galaxy.

TABLE 1

MOLECULAR CLOUDS NEAR $l = 125°$ AND $l = 220°$

Cloud Number	V_r (km s^{-1})	l[a]	b[a]	N_{det}[b]	$\langle T_R^* \rangle$[c] (K)	T_R^* (K)	$\langle \Delta V \rangle$[c,d] (km s^{-1})	$\langle T_R^* \Delta V \rangle$[c,d] (K km s^{-1})
1........	−18	125°400	2°067	2	1.3	1.4	1.8	2.5
2........	−53	125.600	2.067	15	3.9	7.7	2.5	11.1
3........	−58	124.667	2.200	1[e]	0.8	0.8	1.3	1.2
4........	−58	125.467	1.067	3	1.7	2.1	2.6	4.5
5........	−59	125.867	2.333	2	1.4	1.5	1.4	2.3
6........	−61	124.133	2.200	2	1.2	1.3	2.6	3.4
7........	−61	125.067	2.867	7	2.2	2.9	2.5	6.3
8........	−65	125.800	1.667	6[e]	2.5	3.4	2.4	6.8
9........	−71	124.400	1.867	12	1.9	3.2	2.4	5.1
10........	−78	124.467	2.200	2	1.5	1.9	2.6	3.2
11........	−87	125.467	2.267	2	1.4	1.5	...	...
12........	−94	124.200	2.117	1[e]	1.6	2.2	1.5	3.0
13........	+13	220.333	−2.200	74	3.5	6.8	1.9	7.8
14........	+27	217.967	−0.783	3	1.8	2.4	4.3	7.8
15........	+32	220.067	−2.000	15	2.1	2.7	2.5	5.3
16........	+32	220.267	−2.600	2	2.0	2.3	1.7	4.4

[a] Position at center, not peak, of detected emission.
[b] Number of lines detected on a grid of 1′ spacing for cloud 14 and 4′ spacing for all other clouds.
[c] Average over cloud.
[d] Numbers obtained by Gaussian fits to line profiles.
[e] Additional mapping with 1′ grid spacing.

not determined by further mapping. Because of the coarseness of the 4′ grid spacing compared with the 1′.1 beam, small angular size clouds have less accurate diameters than clouds detected at many positions. The relative error, however, is made smaller by using the diameter instead of the measured cloud surface area in the analysis.

The cloud surface area is determined by assigning to each grid point detected an angular cloud surface area of 4′ × 4′ and 1′ × 1′, as appropriate. The diameter is then defined as the square root of the cloud surface area, and should give a reasonable statistical measure of the cloud size.

We strive to use a well-defined and uniform subsample of clouds when we derive a size spectrum in § V by comparing data with the models. We therefore excluded clouds with diameters less than the grid spacing, namely, clouds 3 and 12, because such small clouds require large incompleteness corrections.

Clouds that overlap the survey boundary require special consideration in order not to bias the analysis; large clouds lying outside the survey boundary will contaminate the survey more frequently than small clouds. The most straightforward criterion to apply as part of a statistical analysis is to include only those clouds whose centers fall inside the survey boundary. Except for cloud 5, additional mapping of boundary-crossing clouds was done to determine cloud diameters and central positions. We included cloud 5 in the subsample, judging from its shape and low temperature that the cloud probably does not extend past the survey boundary.

TABLE 2

SIZE AND DISTANCE OF OUTER GALAXY MOLECULAR CLOUDS

			BFS ROTATION CURVE			FLAT ROTATION CURVE		
CLOUD NUMBER	V_r (km s^{-1})	$\langle b \rangle_{\rm H\,I}$[a]	$\mathfrak{d}$[b] (pc)	r (kpc)	R (kpc)	$\mathfrak{d}$[b] (pc)	r (kpc)	R (kpc)
1........	−18	0°22	2.2	1.3	10.8	2.6	1.5	11.0
2........	−53	1.54	23.9	5.3	13.7	22.5	5.0	13.5
3........	−58	1.58	7.1	8.7	16.5	4.6	5.6	14.0
4........	−58	1.84	17.5	8.7	16.5	11.3	5.6	14.0
5........	−59	1.88	>15.4	9.4	17.1	>9.4	5.7	14.0
6........	−61	1.80	16.2	9.8	17.5	9.7	5.9	14.2
7........	−61	1.81	30.2	9.8	17.5	18.2	5.9	14.2
8........	−65	1.88	29.0	10.2	17.8	18.2	6.4	14.6
9........	−71	1.59	43.2	10.7	18.3	29.0	7.2	15.3
10........	−78	1.53	19.5	11.8	19.3	13.5	8.2	16.1
11........	−87	2.47	22.2	13.5	20.8	15.8	9.6	14.4
12........	−94	1.69	8.7	14.9	22.1	6.3	10.8	18.5
13........	+13	−2.94	>10.0	1.0	10.8	>11.2	1.1	10.9
14........	+27	−0.73	>3.7	1.8	11.5	>5.0	2.5	12.0
15........	+32	−1.16	11.4	2.5	12.1	13.5	3.0	12.5
16........	+32	−1.20	4.4	2.7	12.2	5.1	3.1	12.5

[a] Latitude of H I midplane for given l, V_r.
[b] Cloud diameter $\mathfrak{d} = r\theta_{gr} N_{det}^{1/2}$, where θ_{gr} is the angular grid spacing and N_{det} is from Table 1.

We found that two boundary-crossing clouds, both in the third quadrant, had cloud centers lying outside the survey boundary. This is not surprising, in the sense that the third-quadrant field samples a nearby spiral arm where clouds can be expected to have large angular sizes. However, this leads to the exclusion of two out of only four third-quadrant clouds and to the difficulty that models calculated for the third quadrant cannot be usefully compared with only two clouds. An alternative strategy would be to compare the combined second- and third-quadrant cloud data to the combined second- and third-quadrant models. However, simply adding a poorly constrained third-quadrant model to the second-quadrant model could easily give rise to a systematic bias in the results; we deemed the gain of two clouds to the subsample insufficient to warrant including the third-quadrant data in the model analysis. A total of 10 clouds, detected with a 4′ spacing, comprises the data subsample.

III. LARGE-SCALE STRUCTURE IN THE OUTER GALAXY

a) Antenna Temperatures and the ^{12}CO/^{13}CO *Ratio*

Shown in Table 1 are the ensemble properties of the cloud sample, such as the characteristic cloud temperature $\langle T_R^* \rangle$, i.e., T_R^* averaged over each cloud, and the peak cloud temperature. In addition, Gaussian profiles were fitted to the lines in order to estimate ΔV, the velocity width, and $T_R^* \Delta V$, the integrated line profile. Although there is a trend for the most distant clouds to have somewhat lower antenna temperatures, this may simply be the effect of beam dilution, since all the small angular size clouds have low temperatures regardless of their distance. Outer Galaxy clouds have low characteristic temperatures, as can also be seen in the data of Solomon, Stark, and Sanders (1983). For the cloud ensemble, average values are 2.3 km s^{-1} for ΔV and 5.0 K km s^{-1} for the integrated line profile. We leave open the question of whether a cloud population of even lower intensity and/or narrower lines is prevalent, since our values for characteristic line temperatures and velocity widths are near our detection limits. These clouds differ from the inner Galaxy cloud sample of Sanders, Scoville, and Solomon (1985), who quote typical peak temperatures of 3–6 K and velocity widths (FWHM) between 5 and 10 km s^{-1}. The clouds have properties similar to those of the high-latitude solar neighborhood clouds studied by Blitz, Magnani, and Mundy (1984), except for the small size (2 pc) of the high-latitude clouds.

A small number of ^{13}CO spectra were obtained in order to investigate the ratio of ^{12}CO to ^{13}CO emissivities. We estimated the ratio of the integrated line profiles using $\mathscr{R} = T_R^* \Delta V(^{13}\text{CO})/T_R^* \Delta V(^{12}\text{CO})$. Measured values of $\mathscr{R}$ ranged from 5 to 15, with a number of upper limits. If we define our detection criterion for a ^{13}CO line to be $3\ \sigma \times 2$ channels, where σ is the rms noise level per frequency channel, then the median detection limit for $\mathscr{R}$ was 9.8 for our sample. A total of 9 out of 23 spectra, somewhat less than half, resulted in detections, implying that the average ratio $\langle \mathscr{R} \rangle$ is somewhat larger than 9.8. This is larger than the average value of 5.5 quoted by Sanders, Solomon, and Scoville (1984) but close to the local high-latitude cloud value of 10.5 given by Blitz, Magnani, and Mundy (1984). The trend toward higher values of the ^{12}CO to ^{13}CO ratio $\mathscr{R}$ in the outer Galaxy is consistent with the factor of 2 increase found by Liszt, Burton, and Xiang (1984) between the peak of the molecular ring and the solar circle.

b) Galactic Warp

In agreement with Fich and Blitz (1984) for H II regions, we find that the molecular emission follows the warp seen in the H I gas. Figure 3 shows the position of the H I midplane near $l = 125°$ in the observational coordinates of latitude versus radial velocity. The positions of molecular cloud centers are also plotted. Detected emission clusters near the midplane and a gap in detections occurs at velocities near -35 km s^{-1}, where the midplane drops outside our survey limits. The one seemingly discrepant point at -18 km s^{-1} is nearby (1.3 kpc) and so lies only 42 pc away from the midplane.

c) Spiral Arms

The number density of molecular clouds is enhanced in the spiral arms, as can be seen indirectly from Figure 3. Over the velocity range -53 to -100 km s^{-1}, where the H I midplane lies inside the survey boundary and where the bulk of the clouds were detected, one can see that half of the detected clouds fall in the range -58 to -65 km s^{-1}. This correlates well with the peak of the emission in H I near $l = 125°$ that is part of the Perseus arm.

IV. MODELS

a) Method

For a complete cloud sample, i.e., a sample where clouds of different sizes can be detected equally well throughout the sample volume, one can calculate the shape of the size spectrum directly from the data. In order to include small clouds that are incompletely sampled in the analysis, it is necessary to construct a model of the smaller effective volume that is sampled as a function of cloud size, i.e., the incompleteness correction. After a model is calculated, we use statistical methods to fit the model to the data and to estimate the goodness of fit. First, we use the maximum likelihood technique (Alexander 1961) to determine the parameters of the best-fitting model. We then use the Kolmogorov-Smirnov statistic (Hoel, Port, and Stone 1971) to indicate the reliability of the fit. We construct 90% confidence bands from the data for the two cumulative marginal distributions, i.e., the number of clouds versus cloud size and the number of clouds versus line-of-sight distance. The cumulative distribution of the real underlying process then is bracketed by the confidence limits with a 90% probability. In the remainder of this section we discuss how we construct the model.

b) Summary of Model

The observed sample of clouds $n_{\text{obs}}(\mathfrak{d}, \boldsymbol{R})$ is related to the joint cloud size and space density $n(\mathfrak{d}, \boldsymbol{R})$ by

$$n_{\text{obs}}(\mathfrak{d}, \boldsymbol{R}) = n(\mathfrak{d}, \boldsymbol{R}) p_{\text{det}}(\mathfrak{d}, \boldsymbol{R}) , \tag{1}$$

where $n(\mathfrak{d}, \boldsymbol{R})$ is the number of clouds per unit volume per unit cloud diameter and $p_{\text{det}}(\mathfrak{d}, \boldsymbol{R})$ is the probability that the telescope survey will detect clouds of diameter $\mathfrak{d}$ and position $\boldsymbol{R}$. If we assume that the cloud size spectrum is independent of position, then $n(\mathfrak{d}, \boldsymbol{R}) = n_{\mathfrak{d}}(\mathfrak{d}) n_v(\boldsymbol{R})$, where $n_{\mathfrak{d}}$ is the cloud size spectrum and n_v is the cloud space density. In principle, by using a large enough sample, one can invert equation (1) to obtain the cloud size spectrum and space density from the observed distribution. For small samples, however, it is better to compare models of the Galactic molecular cloud density $n(\mathfrak{d}, \boldsymbol{R})$ with the observations.

To specify $n_v(\boldsymbol{R})$, we adopt a simple model for the outer

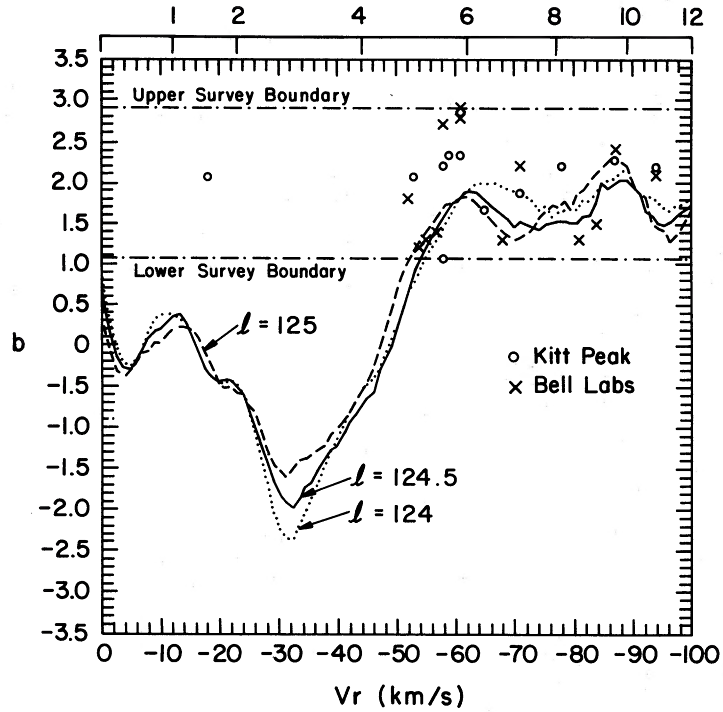

FIG. 3.—Position of the H I midplane toward the directions $l = 124°$, $124°.5$, and $125°$ is plotted in the observational coordinates of latitude b against radial velocity V_r. The top scale shows line-of-sight distances assuming a flat rotation curve. The survey boundaries are indicated by dot-dash lines. Open circles mark the positions of cloud centers from the Kitt Peak data, while crosses mark spectral line detections from the Bell Laboratories data. Molecular clouds are seen to cluster near the H I midplane, with a gap in detections occurring where the midplane drops below the survey boundary. The one seemingly discrepant point is nearby and actually lies close to the midplane.

Galaxy, described in more detail in § IV*c*, that the molecular gas follows the H I midplane with some perpendicular Gaussian scale height σ_z and that the gas midplane density is constant except for a density enhancement that is allowed in spiral arms with some contrast ratio f_{cr}. The models are not sensitive to the small range in reasonable values of σ_z but do vary with the parameter f_{cr}.

The choice of rotation curve is a component of the model in that kinematic distances are assigned to the observed molecular clouds and also to the position of the H I midplane. We use the BFS rotation curve and also compute models using a flat rotation curve with $R_\odot = 10$ kpc and $\theta_\odot = 250$ km s^{-1} for comparison.

The cloud detection probability $p_{det}(\mathfrak{d}, \boldsymbol{R})$ describes the incompleteness that occurs for clouds close to and smaller than the survey grid spacing and is derived in § IV*d*. It results from the ability to detect large clouds out to a greater distance and in a larger volume than small clouds. Because many of the ^{12}CO lines we observed were close to the survey detection limit and thus contained substantial amounts of random noise, we have chosen not to include the antenna temperature distribution in our analysis. In effect, the results we derive from the model will hold for those clouds with antenna temperatures greater than the survey detection threshold.

c) Model of Molecular Cloud Density

We choose a simple power-law functional form to represent the cloud size spectrum $n_\mathfrak{d}$, where

$$n_\mathfrak{d}(\mathfrak{d}) = \left[\frac{\mathfrak{d}}{\mathfrak{d}_0}\right]^\alpha, \quad \mathfrak{d}_{min} \le \mathfrak{d} \le \mathfrak{d}_{max}. \qquad (2)$$

We scale the size spectrum to $\mathfrak{d}_0 = 30$ pc, a value for which selection effects are not usually important in most surveys. We set $\mathfrak{d}_{min} = 1$ pc and $\mathfrak{d}_{max} = 50$ pc in order to bracket the observed minimum and maximum cloud diameters. There is not too great a difference between a power law with a maximum cutoff and a pure power law for the relevant values of α less than -2 since the integral of the size spectrum over cloud diameter differs by less than 2% for the values $\mathfrak{d}_{max} = 50$ pc and $\mathfrak{d}_{max} = \infty$. The model is not sensitive to the specific value of $\mathfrak{d}_{min}$, since very small and local clouds are automatically excluded through the function $p_{det}(\mathfrak{d}, \boldsymbol{R})$. The parameter α is varied in the model-fitting procedure.

The cloud space density, $n_v(\boldsymbol{R})$, is represented by

$$n_v(\boldsymbol{R}) = n_r(r, l) n_z(z, r, l), \qquad (3)$$

where $n_z(z, r, l)$ is the variation of the cloud density perpendicular to the Galactic plane and $n_r(r, l)$ is the cloud density in the CO midplane. We choose a Gaussian form for the z-distribution,

$$n_z(z, r, l) = \exp\left[-\frac{(z - \langle z_{\rm H\,I}\rangle)^2}{2\sigma_z^2}\right], \qquad (4)$$

where $\langle z_{\rm H\,I}\rangle$ is the mean plane defined by the H I gas at the position (r, l). For the position of the mean midplane we use the results of Kulkarni, Blitz, and Heiles (1982). The midplane data have a resolution of $0°.5$ in longitude and about 2.1 km s^{-1} in velocity.

For the cloud density in the plane, $n_r(r, l)$, we choose constant density n_0 plus a feature suggested by the data, a spiral arm with arm-to-interarm contrast ratio f_{cr}. The assumption

n_0 = constant is adequate over the range of galactocentric radii present in the data, given our small-number statistics; to show this, we relax the assumption by allowing a radial decrease in n_0 for some of the models presented in § V. The form of $n_r(r, l)$ is specified by

$$n_r(r, l) = n_0\left[1 + (f_{cr} - 1)\Pi\left(\frac{R - R_m}{R_w}\right)\right] . \quad (5)$$

The value of n_0 gives the absolute scaling in the interarm region of the number of clouds per unit volume per cloud diameter in units of clouds kpc^{-4}. The parameter f_{cr} is allowed to vary from 1 (no spiral arm) to greater than 1 in the model-fitting procedure.

$\Pi(x)$ is a box function defined by

$$\Pi(x) = \begin{cases} 0, & |x| > 0.5 , \\ 1, & |x| \le 0.5 . \end{cases}$$

The variable R is the galactocentric distance, while the parameter R_m is the distance to the spiral arm midpoint and R_w is the galactocentric width of the arm. It should be noted that a given width of the Perseus spiral arm in velocity space translates to a spatial width that is smaller for the flat rotation curve. To compensate partially for this, R_w was given the value of 2 kpc for the BFS rotation curve case and a value of 1 kpc for the flat rotation curve. This further means that a BFS rotation curve model with $f_{cr} = N$ is equivalent to a flat rotation curve model with $f_{cr} = 2N$, in the sense that both predict about the same number of clouds in a spiral arm.

Because the longitude coverage of the survey is small, we did not include the azimuthal inclination of the arm in the model. R_m was estimated from the data for the Perseus arm in the second quadrant.

We correct for the two different sensitivities present in the second quadrant data, with rms noise levels of 0.42 and 0.78 K, by giving empirical weights of 1.0 or 0.17, respectively, to the model for each line of sight that was observed. The relative weight was estimated from the ratio of cloud detections for the different data subsamples (see Fig. 2).

d) *Detection Probability* $p_{det}(\mathfrak{d}, \boldsymbol{R})$

At a given distance from the Sun and for a cloud diameter $\mathfrak{d}$ there is some density of clouds $n(\mathfrak{d}, \boldsymbol{R})$. The detection probability $p_{det}(\mathfrak{d}, \boldsymbol{R})$ is a number between 0 and 1 representing the fraction of clouds that will actually be detected because of the choice of the survey sampling grid, the beam size, and limited sensitivity of the instrument. Here we assume that the reservoir of clouds $n(\mathfrak{d}, \boldsymbol{R})$ contains those clouds having brightness temperatures greater than the detection limit of the survey, $T_{3\sigma}$.

If a cloud has an angular diameter much larger than the beam size, then detection occurs when at least one line of sight intersects the cloud. For this case the detection probability is calculated by determining the geometrical blind spots of the survey grid. When the cloud angular diameter becomes comparable to the beam size, then the brightness temperature also affects detection, since the cloud very rarely overlaps the entire beam. Hotter clouds will be detected preferentially. In principle, the cold clouds missed could be estimated if the cloud temperature distribution was known. A further complication arises if brightness temperature is a function of size; for example, if hotter clouds tend to be larger as well, this introduces a bias in favor of large clouds. In the absence of enough information to correct for the brightness temperature dependence, we purposely limit our analysis to clouds larger than the beam size, namely, to clouds with angular diameter larger than the grid spacing in a coarsely sampled survey.

In order to calculate $p_{det}(\mathfrak{d}, \boldsymbol{R})$, we make the idealizations that (1) the projection of a cloud on the sky is circular in shape and has uniform brightness temperature, (2) the telescope beam is circular with uniform sensitivity inside the half-power radius, and (3) a detection occurs only if the cloud overlaps the entire beam.

Let θ_{gr}, θ_{be}, θ_{cl} be one-half the grid spacing on the sky, the HWHM powerpoint of the beam, and the angular cloud radius, respectively. Then let the corresponding solid angle on the sky be given by

$$\Omega_{gr} = 4\theta_{gr}^2 , \quad \Omega_{be} = \pi\theta_{be}^2 , \quad \Omega_{cl} = \pi\theta_{cl}^2 .$$

The detection probability is then given by

$$p_{det}(\mathfrak{d}, \boldsymbol{R}) = \frac{\Omega_{det}}{\Omega_{gr}} , \quad (6)$$

where the solid angle Ω_{det} is defined to include all points where a cloud center occurring at that point results in a detection.

The detection probability equals unity for clouds larger than some angular radius θ_{comp}. The clouds that are most difficult to detect have cloud centers at the midpoint of the diagonal between two grid points (see Fig. 4, *upper panel*). Positive detection occurs for $\theta_{cl} > \theta_{comp}$, where

$$\theta_{comp} = (\surd 2)\theta_{gr} + \theta_{be} , \quad p_{det}(\theta_{cl} > \theta_{comp}) = 1 . \quad (7)$$

The smallest clouds we consider are those with a cloud radius $\theta_{min} = \theta_{gr} + \theta_{be}$. A cloud with radius θ_{min} whose center lies within radius $\theta = \theta_{gr}$ of a grid point will be detected, so

$$p_{det}(\theta_{cl} = \theta_{min}) = \frac{\pi\theta_{gr}^2}{\Omega_{gr}} = \frac{\pi}{4} , \quad \theta_{min} = \theta_{gr} + \theta_{be} . \quad (8)$$

For clouds $\theta_{min} \le \theta_{cl} \le \theta_{comp}$ (see Fig. 4, *lower panel*) the detection probability is given by

$$p_{det}(\theta_{min} \le \theta_{cl} \le \theta_{comp}) = \left(\frac{\pi}{4} - \phi\right) \sec^2 \phi + (\sec^2 \phi - 1)^{1/2} , \quad (9a)$$

where

$$\phi = \arccos\left(\frac{\theta_{gr}}{\theta_{cl} - \theta_{be}}\right) , \quad 1 \le \sec \phi \le \surd 2 . \quad (9b)$$

The detection probability can be calculated in a similar fashion for clouds with $\theta_{cl} < \theta_{min}$: however, its value quickly approaches zero, and in a way that depends on the assumptions used to derive it. Our approach was to exclude clouds smaller than θ_{min} from our observational cloud sample. This formally implies $p_{det}(\theta_{cl} < \theta_{min}) = 0$. Unfortunately, this leads to a computationally undesirable discontinuity at $\theta_{cl} = \theta_{min}$. We have therefore added an ad hoc exponential cutoff for $\theta_{cl} < \theta_{min}$ that ensures continuity but does so without significantly affecting the model results.

V. RESULTS

In this section we compare the models with the molecular cloud data in order to derive the cloud size spectrum and the relative strength of the spiral arms. The models, described in

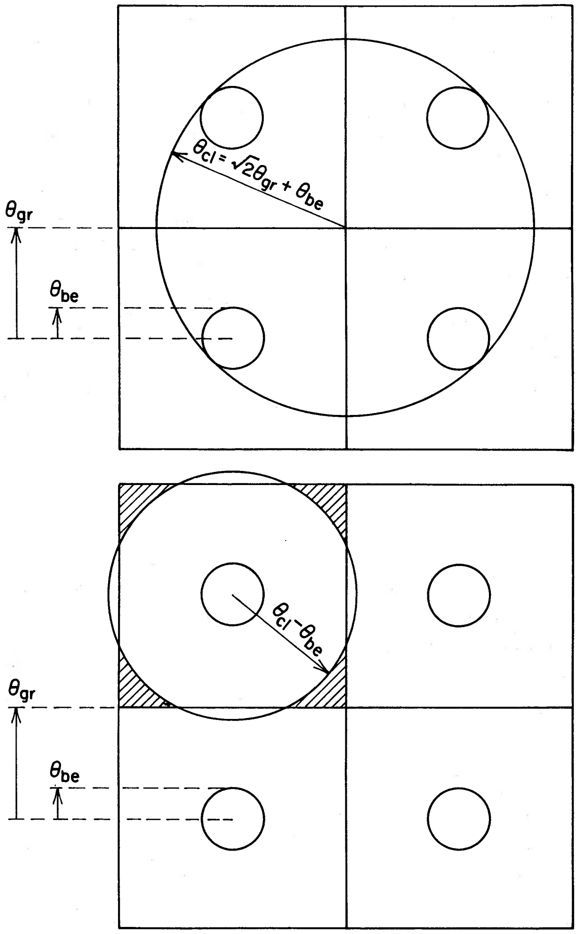

FIG. 4.—Figures illustrate the theoretical likelihood of detecting a cloud of angular radius θ_{cl} when using a telescope with angular beam radius θ_{be} and survey grid spacing $2\theta_{gr}$. *Top*: Shown is the smallest cloud that will be detected in at least two grid points with 100% probability. *Bottom*: A cloud of angular radius $\theta_{cl} < (\sqrt{2})\theta_{gr} + \theta_{be}$ will not be detected if its center lies within the hatched region.

detail in § IV, calculate $n_{obs}(\mathfrak{d}, \boldsymbol{R})$, which is the observed cloud density per unit volume per unit cloud diameter.

Two different rotation curves were used; we refer to the flat rotation curve as case A and to BFS as case B. The two rotation curves probably give a good indication of the uncertainty in the outer Galaxy rotation curve, and we use them to indicate the level of sensitivity of the model results to the choice of rotation curve. The known velocity anomaly of 20–30 km s^{-1} in the Perseus arm introduces an uncertainty in our results that is of the same order as the choice of rotation curve.

In order to determine the best-fitting model, we have constructed the maximum likelihood function for cases A and B and for different values of the spiral arm contrast ratio f_{cr} and the size spectrum index α. The best-fitting model is that model having the maximum value of the maximum likelihood function.

The log of the maximum likelihood function is plotted against the size spectrum index α in Figures 5*a* and 5*b*. The models use a value of the vertical Gaussian scale height σ_z equal to 85 pc, corresponding to a HWHM of 100 pc. The models themselves are very insensitive to different choices for the scale height. The apparent offset between cases A and B is not real, and comes about because the value of the maximum likelihood function is not invariant to coordinate transformations. Cases A and B should therefore be considered separately when interpreting Figure 5.

In Figure 5*a* the value of the maximum likelihood function is seen to vary more with the value of the power-law index α than with the parameter f_{cr}. The maximum ordinate value α_{ML} for case A is -2.8 with $f_{cr} = 4$; for case B it is -2.6 with $f_{cr} = 6$. The entire range of α_{ML} in Figure 5*a* is about -2.4 to -2.8, showing that the best-fitting value of α_{ML} is fairly insensitive to the choice of the rotation curve and the details of the model of the molecular cloud space density.

To further expand on this point, we relax the somewhat artificial assumption of constant cloud surface density. We have calculated a sequence of models that incorporate a radial decrease in the cloud spatial density n_0 in order to show the resultant magnitude and direction of change in the value of α_{ML}. We do this because, unfortunately, current observational data do not allow us to set good *a priori* constraints on the radial decrease in surface density appropriate to our survey. We note that available information (Sanders, Solomon, and Scoville 1984) suggests a surface density decrease in the neighborhood of a factor of 4.

Figure 5*b* shows a series of models with a radial linear decrease in cloud surface density ranging from 1 (no radial decrease) to 8. First notice that the maximum value of the ordinate changes little, showing that the significance of the fit is not sensitive to the radial surface density. Better *a priori* information is needed to specify the best model.

The largest effect introduced by the radial surface density decrease is to shift the peak in α by 0.3 to a shallower power law. This reflects an uncertainty at the same level as that due to the choice of rotation curve and furthermore gives a value that lies within our 90% confidence limits. Finally, we note that the shift to a shallower power law strengthens the conclusions we draw in § VI.

We display the n_0 = constant models by showing the marginal and cumulative distributions of clouds versus line-of-sight distance and clouds versus cloud diameter. Models for case A with $f_{cr} = 4$ and for case B with $f_{cr} = 6$ are shown in Figures 6 and 7, respectively. The smooth curves seen in all the figures represent models with values of the power-law index α ranging from 0 to -4.

The marginal distribution $p_{\mathfrak{d}}(\mathfrak{d})$, i.e., the number of clouds per unit cloud diameter, is shown in Figures 6*a* and 7*a* and is defined by

$$p_{\mathfrak{d}}(\mathfrak{d}) = \frac{\int_V n_{obs}(\mathfrak{d}, \boldsymbol{R}) d\boldsymbol{R}}{\int_{\mathfrak{d}_{min}}^{\mathfrak{d}_{max}} \int_V n_{obs}(\mathfrak{d}', \boldsymbol{R}) d\boldsymbol{R} d\mathfrak{d}'} , \tag{10}$$

where V is the survey volume. The marginal density $p_{\mathfrak{d}}(\mathfrak{d})$ has the units of clouds per kiloparsec and is normalized to equal unity when integrated over cloud diameter. The effects of incompleteness can be seen by examining the $\alpha = 0$ curve. In the absence of selection effects, the curve would be horizontal. For clouds smaller than about 20 pc the fraction of clouds that are detected quickly drops. Most of the incompleteness arises from the fact that small clouds can be detected only in a subset of the entire survey volume; the effective sample volume decreases roughly as R_{lim}^3, where $R_{lim} = \mathfrak{d}/\theta_{gr}$. As can be seen from Figure 6*a*, a steep power law ensures that many small clouds will be detected despite the action of selection effects. In addition, note that any analysis that includes small clouds

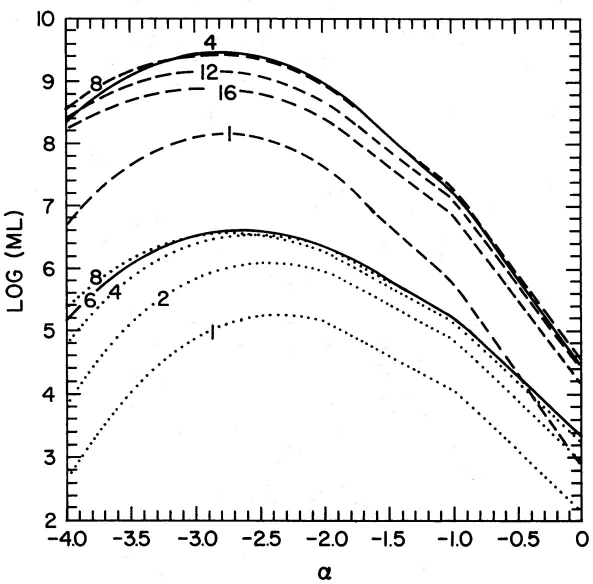

FIG. 5a

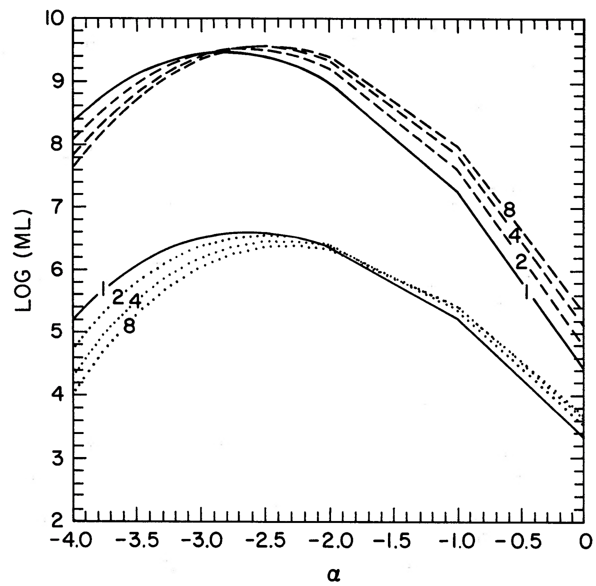

FIG. 5b

FIG. 5.—The log of the maximum likelihood function is plotted against the cloud size power-law index α. Both flat rotation curve models (*dashed lines*) and BFS rotation curve models (*dotted lines*) are shown. (*a*) Curves are labeled by different values of the spiral arm contrast ratio f_{cr}. The maximum value attained by the ordinate determines the best-fitting model (*solid lines*). Thus, the best fit is $\alpha_{ML} = -2.8, f_{cr} = 4$ for a flat rotation curve, and $\alpha_{ML} = -2.6, f_{cr} = 6$ for the BFS rotation curve. Notice that the maximum likelihood value of α is insensitive to the choice of rotation curve and the spiral arm contrast ratio. The apparent offset between cases A and B is an artifact of the method. (*b*) Models with $f_{cr} = 4$ for a flat rotation curve and $f_{cr} = 6$ for the BFS rotation curve are shown. Curves are labeled by different values of the surface density variation defined by $n_0(R_{min})/n_0(R_{max})$ and ranging in value from 1 (n_0 = constant) to 8.

without correcting the observed distribution for selection effects will systematically derive a flatter cloud size spectrum than is actually present. The detailed features seen in the models reflect variations of the spatial cloud density, i.e., the spiral arms and the change in the H I midplane.

The cumulative distribution $P_{\mathfrak{d}}(\mathfrak{d}' \geq \mathfrak{d})$ is plotted in Figures 6*b* and 7*b*, where

$$P_{\mathfrak{d}}(\mathfrak{d}' \geq \mathfrak{d}) = \frac{\int_{\mathfrak{d}_{min}}^{\mathfrak{d}_{max}} \int_V n_{obs}(\mathfrak{d}', \boldsymbol{R}) d\boldsymbol{R} d\mathfrak{d}'}{\int_{\mathfrak{d}_{min}}^{\mathfrak{d}_{max}} \int_V n_{obs}(\mathfrak{d}', \boldsymbol{R}) d\boldsymbol{R} d\mathfrak{d}'} , \quad (11)$$

and where $P_{\mathfrak{d}}$ represents the probability that a cloud will have a diameter $\mathfrak{d}' \geq \mathfrak{d}$. The cloud data are plotted in histogram form. The fit to the data is reasonable, but it should be kept in mind that the maximum likelihood method uses information from the joint density $n_{obs}(\mathfrak{d}, \boldsymbol{R})$, which may give a result that does not exactly correspond to an eyeball fit of the marginal density; this is because the marginal density is constructed by integrating $n_{obs}(\mathfrak{d}, \boldsymbol{R})$ over one coordinate and so inherently contains less information than the joint density. To estimate the reliability of the fit, we plot the 90% confidence bands using the one-dimensional Kolmogorov-Smirnov statistical test for $N_{cl} = 10$. These are indicated by the dashed histograms. From the model curves that lie within the 90% confidence bands we see that values of α in the range $[-1.5, -3.8]$ for case A and $[-0.7, -3.3]$ for case B are consistent with this level of uncertainty.

The marginal density $p_r(r)$ is plotted in Figures 6*c* and 7*c* and is defined by

$$p_r(r) = \frac{\int_\Omega \int_{\mathfrak{d}_{min}}^{\mathfrak{d}_{max}} n_{obs}(\mathfrak{d}', r, \Omega') r^2 d\mathfrak{d}' d\Omega'}{\int_V \int_{\mathfrak{d}_{min}}^{\mathfrak{d}_{max}} n_{obs}(\mathfrak{d}', \boldsymbol{R}') d\mathfrak{d}' d\boldsymbol{R}'} , \quad (12)$$

where Ω is the angular coverage of the survey in steradians. The strong feature present is the Perseus spiral arm. The jaggedness apparent in the curves occurs because the models depend on an observational quantity, the position of the H I midplane, which has some noise associated with it.

The cumulative probability distribution $P_r(r' < r)$ is shown in Figures 6*d* and 7*d* and is defined by

$$P_r(r' \leq r) = \frac{\int_{r_{min}}^{r} \int_\Omega \int_{\mathfrak{d}_{min}}^{\mathfrak{d}_{max}} n_{obs}(\mathfrak{d}', r', \Omega') r'^2 dr' d\Omega' d\mathfrak{d}'}{\int_V \int_{\mathfrak{d}_{min}}^{\mathfrak{d}_{max}} n_{obs}(\mathfrak{d}', \boldsymbol{R}') d\mathfrak{d}' d\boldsymbol{R}'} , \quad (13)$$

and represents the probability that a cloud will occur at a line-of-sight distance $r' \leq r$. The data show a sharp rise near $r = 6$ kpc and ($r = 9$ kpc in Fig. 7*d*) which we attribute to the presence of the Perseus spiral arm. The fit of the model to the data outside the arm region is reasonable.

The parameter n_0, the absolute scaling of the cloud density, is determined by setting

$$N_{cl} = \int_V \int_{\mathfrak{d}_{min}}^{\mathfrak{d}_{max}} n_{obs}(\mathfrak{d}', \boldsymbol{R}') d\mathfrak{d}' d\boldsymbol{R}' , \quad (14)$$

where $N_{cl} = 10$ is the number of clouds observed in the second quadrant. For cases A and B, n_0 has a value of 800 and 600 clouds kpc^{-4}, respectively, where n_0 has the units of clouds per unit volume per unit cloud diameter.

VI. SUMMARY AND DISCUSSION

a) Molecular Cloud Size Spectrum

To summarize our results on the molecular cloud size spectrum, we find that the best-fitting power law has an index $\alpha = -2.6(+1.9\ -0.7)$ when kinematic distances are calculated using the BFS rotation curve, and a value $\alpha = -2.8(+1.3\ -1.0)$ for a flat rotation curve; 90% confidence limits are given. For clouds larger than $(\sqrt{2})\theta_{gr} r_{max} = 26$ pc (BFS) the survey is complete. An incompleteness correction was calcu-

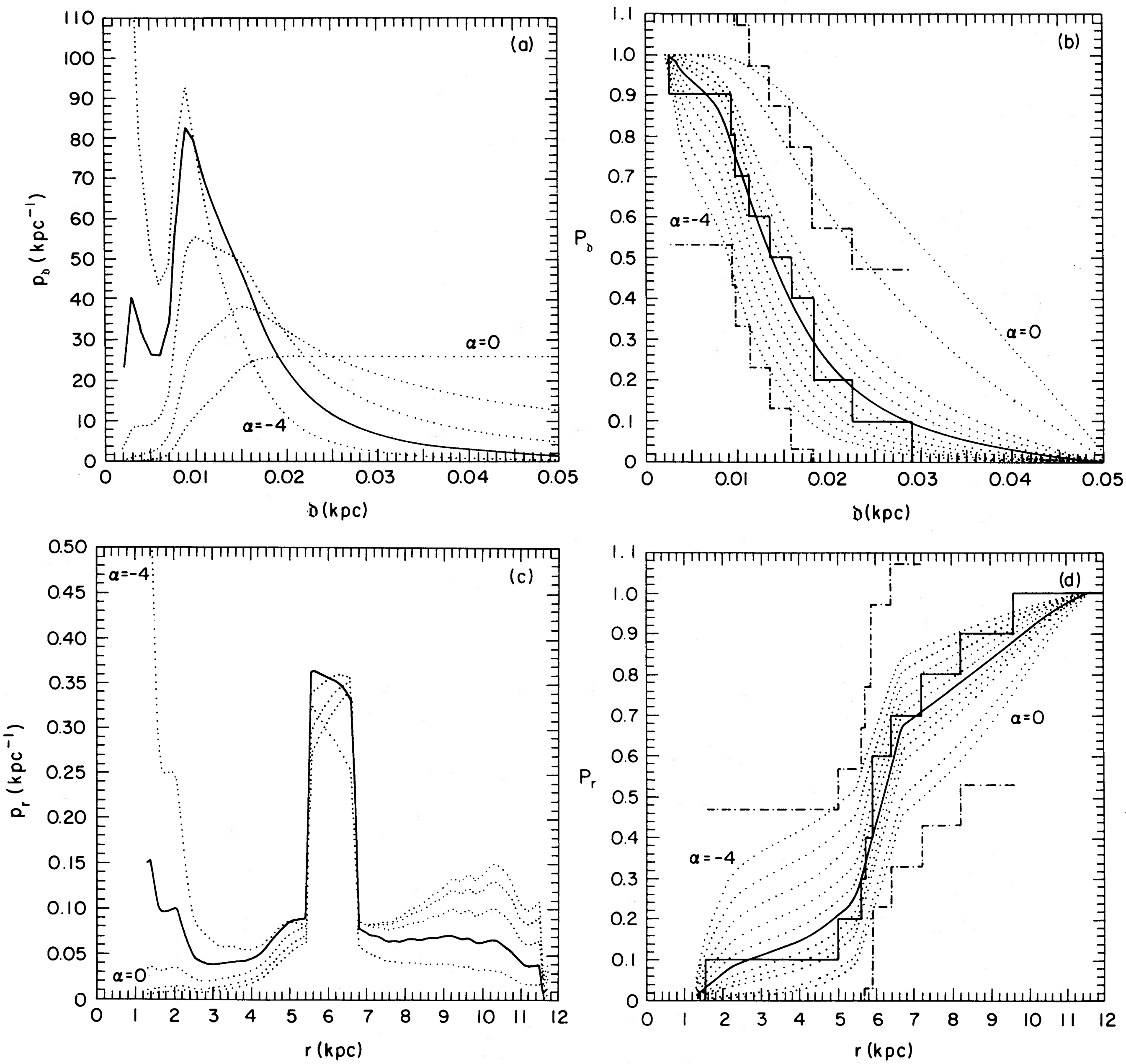

FIG. 6.—Projections of the models are plotted against cloud diameter ƀ or line-of-sight distance r for different values of the parameter α. The models shown use $f_{cr} = 4$ and a flat rotation curve. (*a*) Plot of probability density versus cloud diameter. Model curves with $\alpha = 0, -1, -2, -3, -4$ are shown. The solid curve denotes the $\alpha = -3$ model. (*b*) Plot of cumulative probability versus cloud diameter. Model curves with $\alpha = 0, -1, -2, -2.25, -2{,}5, -2.75, -3, -3.25, -3.5, -3.75, -4$ are shown. The solid curve denotes the $\alpha = -2.75$ model. The solid histogram shows the observational data. The dashed histograms mark the Kolmogorov-Smirnov 90% confidence limits. (*c*) Plot of probability density versus line-of-sight distance. Model curves with $\alpha = 0, -1, -2, -3, -4$ are shown. The solid curve denotes the $\alpha = -3$ model. (*d*) Plot of cumulative probability versus line-of-sight distance. Model curves with $\alpha = 0, -1, -2, -2.25, -2.5, -2.75, -3, -3.25, -3.5, -3.75, -4$ are shown. The solid curve denotes the $\alpha = -2.75$ model. The solid histogram shows the observational data. The dashed histograms mark the Kolmogorov-Smirnov 90% confidence limits.

lated for smaller clouds using the survey grid spacing θ_{gr} and a model for $n_v(\boldsymbol{R})$, the molecular cloud spatial distribution. The derived size spectrum is insensitive to the details of the model $n_v(\boldsymbol{R})$ except for the assumption that the molecular clouds follow the warp seen in the H I gas distribution. However, this assumption is very reasonable, since there is observational evidence seen by us (§ III) and by Fich and Blitz (1984), that the molecular gas follows the H I warp.

A number of other researchers have measured the molecular cloud size spectrum. Solomon, Sanders, and Scoville (1979) find a value of $\alpha = -3.4$ for a sample of chords measured from two longitude strips in the inner Galaxy. The near-far distance ambiguity was treated by assuming all clouds to be at the near distance. This has the effect of making the derived size spectrum steeper than its actual value, as can be seen from the following argument. Suppose that a given velocity corresponds to a near kinematic distance r_1 and a far distance r_2; then a longitude strip of angular size Δl subtends an arc of length $r_1 \Delta l$

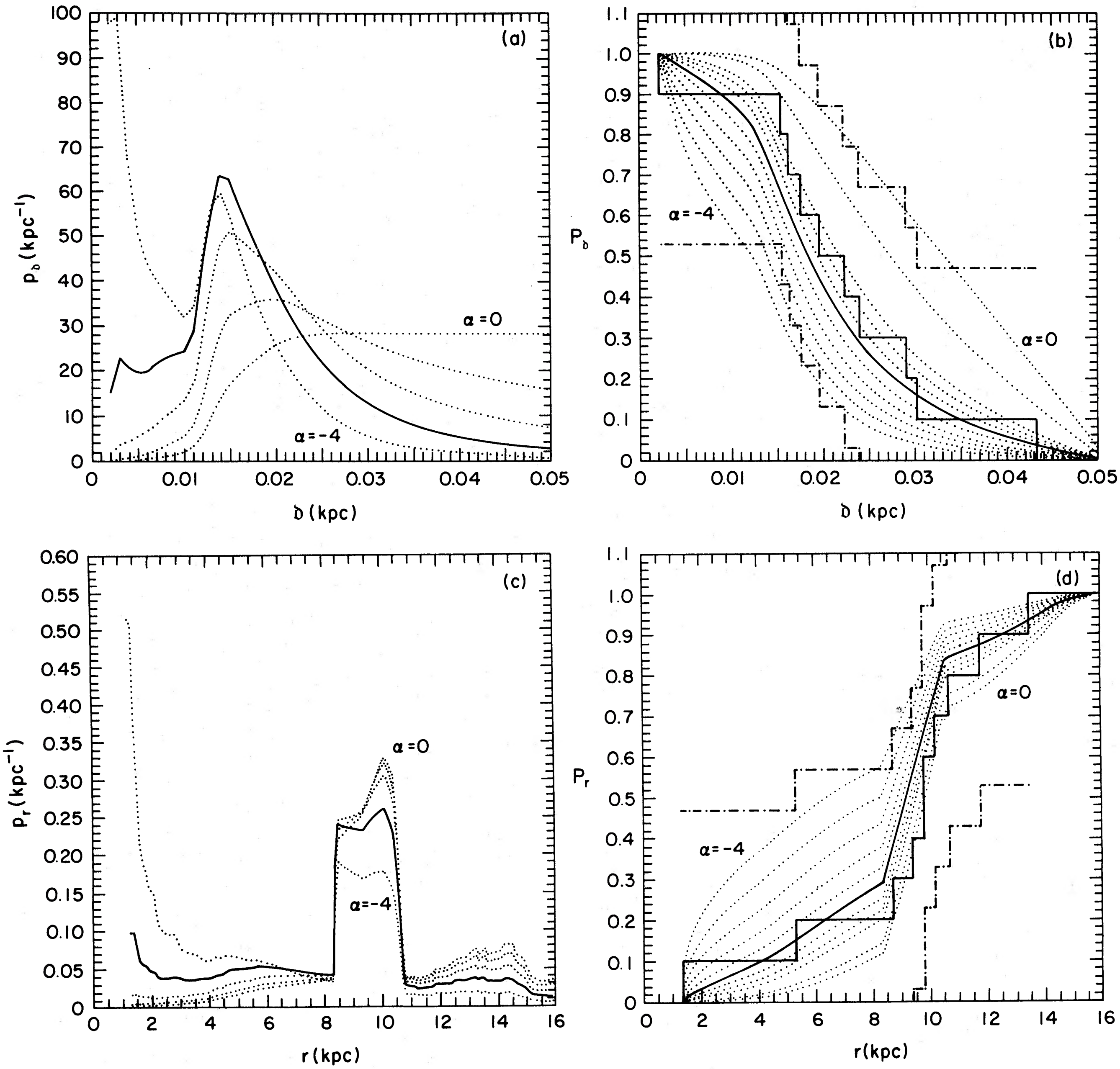

FIG. 7.—Figure descriptions are the same as for Figures 6*a*–6*d*, except that the models shown use a best-fit value of $f_{cr} = 6$ and the BFS rotation curve

and $r_2 \Delta l$ at the near and far distances, respectively. There will therefore be $r_2/r_1 \geq 1$ times more clouds at the far distance than at the near distance; however, the far clouds will have an assigned size r_1/r_2 times smaller than their actual size, leading to a relative overabundance of small clouds in the observed distribution.

Liszt, Xiang, and Burton (1981) have measured a value of $\alpha = -3.3$, also from a sample of cloud chords in the inner Galaxy. They assigned distances to the clouds by assuming that a cloud had even probability of being at the near or far distance, and limited their cloud sample to values of $r_2/r_1 \leq 2$. This compensates for the bias toward a steep size spectrum, but by an unknown amount.

Casoli, Combes, and Gerin (1984) mapped several areas near but outside the solar circle and have derived a value for α of about -2.4 for both their Perseus arm and Orion arm data sets. The near-far kinematic distance ambiguity does not affect distances outside the solar circle and so is not a consideration in their survey. The best result quoted is at the 90% confidence level for the Perseus arm data, with clouds defined using a 4 km s^{-1} wide velocity window. However, there is some cause for the caution because the completeness limit $\mathfrak{d}_{comp} = (\sqrt{2})\theta_{gr} r_{max} = (\sqrt{2})(8')(4.5 \text{ kpc}) = 14.8$ pc is larger than the quoted 13.5 pc average cloud size. Since no completeness correction was included in the analysis, it is to be expected that the derived value of -2.4 is shallower than the true distribution.

Sanders, Scoville, and Solomon (1985) have rederived the size spectrum by measuring chords in the inner Galaxy on a much larger data set and find a new value of -2.3 for α. They resolve the near-far distance ambiguity and confine their cloud sample to mainly near-side clouds by including only high-latitude clouds that would be more than 2 vertical scale heights off the plane if at the far distance. However, incompleteness seems to affect their result: the completeness limit for detecting a chord is slightly different from the completeness criterion for cloud detection and is given by $c_{\rm comp} = 2\theta_{\rm gr} r_{\rm max}$, which for their survey is $c_{\rm comp} = (2)(12')(5.8 \text{ kpc}) = 40$ pc. Since their cloud size bins range from 15 to 85 pc, the effect of incompleteness may be substantial, implying a steeper actual size spectrum than the measured value of -2.3 for α.

We see that previous determinations of the size spectrum have derived values ranging from -2.3 to -3.4 for α, but that systematic biases affect the results, although by unknown amounts. The sense of the biases is such that if one value of α characterized the true cloud size spectrum, then that value of α is bracketed by the measured range of results. However, the results are derived for different cloud size ranges, and in different parts of the Galaxy. The question of whether α may vary with Galactic radius or with cloud size, as for example whether α is different at the large cloud size end, cannot be answered at present.

The ranges on α given for our analysis are the approximate 90% confidence limits on α. At this level of significance and given the probable uncertainties in other authors' measurements, our results in the outer Galaxy show no evidence for a different size spectrum. In addition, the data of Kutner and Mead (1981) show that giant molecular clouds exist in the outer Galaxy and are similar in size to their inner Galaxy counterparts. The five molecular clouds that they map in the first Galactic quadrant lie in the Cygnus arm, with galactocentric distances of 13.6–15.0 kpc and sizes of 60–80 kpc. This implies that molecular cloud formation takes place in a similar manner throughout the Galaxy.

b) A Single Cloud Formation Process?

The mass spectrum implied by the size spectrum can be simply derived. Suppose that the mass of a cloud is related to the size by $m \propto \rho \mathfrak{d}^3$, with $\rho \propto \mathfrak{d}^\beta$. The mass spectrum is then given by $n_m(m) = n_\mathfrak{d}(\mathfrak{d}) \, | d\mathfrak{d}/dm |$, where $n_\mathfrak{d}(\mathfrak{d}) \propto \mathfrak{d}^\alpha$ is the size spectrum. The effects of an upper or lower cutoff on the size distribution can be included but are unimportant to the argument if the maximum cloud size is much larger than the minimum cloud size. The total mass $dM = m n_m(m) dm$ in clouds per logarithmic mass interval is given by $dM/d \log m \propto m^{(\alpha+1)/(\beta+3)+1}$. Notice that this implies that most of the mass will be found in the largest clouds unless $\alpha < -(4 + \beta)$. Given that typical values for β lie between 0 and -0.75 (e.g., Casoli, Combes, and Gerin 1984; Sanders, Scoville, and Solomon (1985), previous measurements of α have shown that most of the molecular gas in our Galaxy resides in the largest clouds. This also seems to hold in the very outer Galaxy, considered by itself; there the lowest value of α that lies in the 90% confidence band occurs near the boundary, where roughly equal contributions are made to the total mass by each logarithmic mass range.

A measurement by Knude (1981*a*, *b*) of the size spectrum for H I clouds, the other important contributor to the mass of the interstellar medium, gives a value of -2.6 for α in the solar neighborhood, very similar to values for the molecular gas. These clouds range from 2 to 10 pc in size and roughly from 1 to 100 $M_\odot$ in mass: Knude's volume limited sample does not contain information on nearby clouds that are larger than 10 pc. This result implies that most of the nearby neutral hydrogen mass lies in the largest H I clouds, but the size and mass of those largest clouds are not really known.

We have discussed a number of similarities in the properties of molecular clouds; in contrast is the marked radial decrease of the molecular mass surface density outward from its peak near 5 kpc, compared with the nearly constant H I mass surface density. The molecular surface density estimates of Sanders, Solomon, and Scoville (1984) show a factor of 40 decrease from the peak of the molecular ring to the average in the outer Galaxy. Making an extrapolation for the peak of the molecular ring, the data of Bloemen *et al.* (1986) suggest a factor of 10–20 decrease. Both measurements document a very substantial decline in the molecular mass surface density. The interstellar medium changes in character; at the peak of the molecular ring half or more of the gas is molecular, while in the outer Galaxy very little of the interstellar gas is in molecular form.

Given that the cloud size spectrum index is nearly the same for atomic and molecular clouds in the solar neighborhood, and that the molecular cloud size spectrum and maximum molecular cloud size are fairly constant throughout the Galaxy, the simplest conclusion is that one physical mechanism is responsible , even in the outer Galaxy, for the formation of interstellar clouds. Furthermore, the large decrease in the ratio of H_2 to H I mass surface densities over the Galaxy is evidence that the cloud formation mechanism is substantially independent of whether the gas is atomic or molecular.

Given the decline in the molecular mass surface density, then a natural consequence of the idea that one physical mechanism is responsible for cloud formation is that giant H I clouds should exist. If we consider the mass spectrum of all clouds, whether atomic or molecular, then the observational data suggest a mass spectrum index such that most of the interstellar mass is in the largest clouds. Near the peak of the molecular ring much of the interstellar mass is observed to be contained in giant molecular complexes. In the outer Galaxy we would expect most of the mass to lie in giant H I complexes. There is some observational evidence in support of giant H I clouds; McGee (1964), McGee and Milton (1964), and more recently Elmegreen (1986) present evidence for H I "superclouds" with characteristic masses near 10^7 $M_\odot$ in the Milky Way and in other local galaxies.

A review of current theories of cloud formation shows that cloud theories fall broadly into two categories: collisional theories that treat clouds as sticky particles that interact through collisions (Kwan 1979; Cowie 1980; Casoli and Combes 1982), and instability theories that appeal to large-scale instabilities to form the largest mass structures observed, namely, giant molecular clouds (Mouschovias, Shu, and Woodward 1974; Blitz and Shu 1980; Jog and Solomon 1984; Balbous and Cowie 1985). The theories of Cowie (1981) and Elmegreen (1982*a*, *b*) are a hybrid of the two classes, since they treat the clouds as a fluid of particles that can become dynamically unstable.

Although cloud formation theories have been developed mainly to explain giant molecular clouds in the inner Galaxy, the theories can also be applied to the mostly atomic environment of the outer Galaxy. In the context of current theories the interstellar mass, either the bulk gas mass or individual cloud mass, plays a primary role, whereas the atomic or molecular state of the gas is subsidiary, appearing only indirectly as in the thermodynamic properties assumed for the interstellar fluid. On the one hand, this means the theories are general enough to apply throughout the Galaxy; but it also means that current theories do not provide an explanation for the small amount of molecular gas in the outer Galaxy. We now focus attention on disk instability theories, since they make some specific predictions for giant interstellar clouds.

As a class, instability theories have many similar characteristics, which unfortunately makes it difficult to distinguish them observationally. Common to all the theories is the property that the wavelength of the instability is of the order of $2\pi H$, where H is the gas scale height; this represents the linear dimension over which the gas can be collected into a complex. Since the gas scale height increases substantially in the outer Galaxy, it may be possible to distinguish between instability theories and collisional theories by observing the spacing between large cloud complexes.

In instability theories the mass of a giant complex scales roughly as ΣH^2, where Σ is the interstellar mass surface density. Since the radial increase in scale height tends to cancel the radial decrease in gas surface density, the mass of a complex may be expected to be a slowly varying function of galactocentric radius. This is consistent with the nearly constant maximum cloud size observed throughout the Galaxy.

Each theory has an instability criterion, dependent on the local properties of the disk, which must be satisfied for the instability to occur. In principle this can be used to test a theory, but, unfortunately, many of the important disk properties are not well known. We merely make the observational point that a theory must predict instability out to a distance of at least 15 kpc to be viable, since giant molecular clouds are observed in the outer Galaxy.

c) *Summary*

To summarize, we present a technique for deriving the interstellar cloud size spectrum that corrects for the incompleteness inherent in observational surveys. We then apply the method to a ^{12}CO survey of the outer Galaxy and compare our results with previous measurements of the cloud size spectrum.

We conclude that the molecular cloud size spectrum, and the observed range of molecular cloud sizes, appear to be the same throughout the Galaxy. Combined with the similarity of the H I size spectrum, this implies that one physical mechanism is responsible for cloud formation. The significant decrease in the ratio of molecular to atomic gas surface densities throughout the Galaxy points out that (1) conditions in the Galactic disk become increasingly unfavorable to molecule formation outside the molecular ring, (2) current theories of cloud formation and evolution are inadequate to predict what the H_2/H I ratio is and why it varies, and (3) in the outer Galaxy most of the gas is atomic and is probably contained in giant H I complexes.

We thank Shri Kulkarni for providing H I midplane values and Dave Sanders for showing us some unpublished outer Galaxy spectra. S. T. thanks Frank Shu for discussions of disk instability theories and Dave Van Buren and Keith MacGregor for helpful comments on the manuscript. This work was partially supported by National Science Foundation grants AST81-14717 and AST83-15276 and a fellowship from the National Aeronautics and Space Administration Graduate Researchers Program.

REFERENCES

Alexander, H. W. 1961, *Elements of Mathematical Statistics* (New York: Wiley), p. 205.
Balbus, S. A., and Cowie, L. L. 1985, *Ap. J.*, **297**, 61.
Blitz, L., Fich, M., and Stark, A. A. 1980, *IAU Symposium 87, Interstellar Molecules*, ed. B. H. Andrew (Dordrecht: Reidel), p. 213 (BFS).
Blitz, L., Magnani, L., and Mundy, L. 1984, *Ap. J. (Letters)*, **282**, L9.
Blitz, L., and Shu, F. H. 1980, *Ap. J.*, **238**, 148.
Bloemen, J. B. G. M., *et al.* 1986, *Astr. Ap.*, **154**, 25.
Burton, W. B. 1976, *Ann. Rev. Astr. Ap.*, **14**, 275.
Burton, W. B., and Gordon, M. A. 1978, *Astr. Ap.*, **63**, 7.
Casoli, F., and Combes, F. 1982, *Astr. Ap.*, **110**, 287.
Casoli, F., Combes, F., and Gerin, M. 1984, *Astr. Ap.*, **133**, 99.
Clemens, D. P. 1985, *Ap. J.*, **295**, 422.
Cowie, L. L. 1980, *Ap. J.*, **236**, 868.
———. 1981, *Ap. J.*, **245**, 66.
Elmegreen, B. G. 1982*a*, *Ap. J.*, **253**, 634.
———. 1982*b*, *Ap. J.*, **253**, 655.
Elmegreen, D. 1986, in preparation.
Fich, M., and Blitz, L. 1984, *Ap. J.*, **279**, 125.
———. 1986, in preparation.
Guibert, J., Lequeux, J., and Viallefond, F. 1978, *Astr. Ap.* **68**, 1.
Henderson, A. P., Jackson, P. D., and Kerr, F. J. 1982, *Ap. J.*, **263**, 116.
Hoel, P. G., Port, S. C., and Stone, C. J. 1971, *Introduction to Statistical Theory* (Boston: Houghton Mifflin), p. 166.
Howard, R. J. 1982, personal communication.
Jog, C. J., and Solomon, P. M. 1984, *Ap. J.*, **276**, 127.
Knude, J. 1981*a*, *Astr. Ap.*, **97**, 380.
———. 1981*b*, *Astr. Ap.*, **98**, 74.
Kulkarni, S. R., Blitz, L., and Heiles, C. 1982, *Ap. J. (Letters)*, **259**, L63.
Kutner, M. L., and Mead, K. N. 1981, *Ap. J. (Letters)*, **249**, L15.
Kutner, M. L., Mundy, L., and Howard, R. J. 1984, *Ap. J.*, **283**, 890.
Kutner, M. L., and Ulich, B. L. 1981, *Ap. J.*, **250**, 341.
Kwan, J. 1979, *Ap. J.*, **229**, 567.
Liszt, H. S., Burton, W. B., and Xiang, D. L. 1984, *Astr. Ap.*, **140**, 303.
Liszt, H. S., Xiang, D., and Burton, W. B. 1981, *Ap. J.*, **249**, 532.
Lockman, F. J. 1979, *Ap. J.*, **232**, 761.
McGee, R. X. 1964, *IAU Symposium 200, The Galaxy and the Magellanic Clouds*, ed. F. J. Kerr and A. W. Rodgers (Canberra: Australian Academy of Sciences), p. 126.
McGee, R. X., and Milton, J. A. 1964, *Australian J. Phys.*, **17**, 128.
Mouschovias, T. C., Shu, F. H., and Woodward, P. R. 1974, *Astr. Ap.*, **33**, 73.
Robinson, B. J., Manchester, R. N., Whiteoak, J. B., Sanders, D. B., Scoville, N. Z., Clemens, D. P., McCutcheon, W. H., and Solomon, P. M. 1984, *Ap. J. (Letters)*, **283**, L31.
Sanders, D. B., Scoville, N. Z., and Solomon, P. M. 1985, *Ap. J.*, **289**, 373.
Sanders, D. B., Solomon, P. M., and Scoville, N. Z. 1984, *Ap. J.*, **276**, 182.
Solomon, P. M., Sanders, D. B., and Scoville, N. Z. 1979, *IAU Symposium 84, The Large-Scale Characteristics of the Galaxy*, ed. W. B. Burton (Dordrecht: Reidel), p. 35.
Solomon, P. M., Stark, A. A., and Sanders, D. B. 1983, *Ap. J. (Letters)*, **267**, L29.
Ulich, B. L., and Haas, R. W. 1976, *Ap. J. Suppl.*, **30**, 247.

LEO BLITZ: Astronomy Program, University of Maryland, College Park, MD 20742

MICHEL FICH: Astronomy Department, University of Washington, FM-20, Seattle, WA 98195

CHRISTIAN HENKEL: Max-Planck-Institut für Radioastronomie, Auf dem Hügel 69, 5300 Bonn 1, Federal Republic of Germany

SUSAN TEREBEY: High Altitude Observatory, National Center for Atmospheric Research, P.O. Box 3000, Boulder, CO 80307